# Topological logical elements based on defect-mediated sound-wave manipulation

Shi-Feng Li, Jie-Yu Lu, Cui-Yu-Yang Zhou, Xin-Ye Zou,* and Jian-Chun Cheng
*Key Laboratory of Modern Acoustics, MOE, Institute of Acoustics, Department of Physics, Collaborative Innovation Center of Advanced Microstructures, Nanjing University, Nanjing 210093, People's Republic of China*

(Received 25 March 2024; revised 25 May 2024; accepted 26 August 2024; published 11 September 2024)

Growing interest in acoustic topological insulators arises from their robust edge states, which are resistant to defects and backscattering. Traditionally, the edge states of topological insulators are believed to be nearly immune to subwavelength-sized defects. As a result, there have been few studies focusing on utilizing defects to enhance wave control. Here, we investigate the impact of introducing periodic defects into acoustic pseudospin systems on the band structures and extend our analysis to nonperiodic structures. We discover that even a single subwavelength defect can significantly affect the topological boundary states, providing a platform for controlling and switching pseudospin edge states using defects. Expanding on this discovery, we develop a broadband topological sound switch (TSS) that achieves a high transmission ratio before and after switching by simply rotating a single scatterer. Additionally, we design three topological logic gates based on this TSS and experimentally verify their functionality. Our theory and experiments demonstrate that the spatial arrangement of defects can serve as a means of manipulating sound waves, potentially advancing acoustic computing and information processing.

DOI: 10.1103/PhysRevApplied.22.034025

## I. INTRODUCTION

Topological insulators have attracted significant interest in condensed matter physics [1–3] due to their unique bulk band-gap properties and robust edge states [4–10] that are immune to backscattering. Recently, the field of topological insulators has expanded beyond condensed matter physics and has become a cross-disciplinary research area. The simplicity and flexibility of classical systems, such as optical [11–15], elastic [16–18], and acoustic systems [19–34], have led to increased interest in applying topological insulator concepts to these systems. The robustness of topological edge states holds great promise for practical applications in photonic and phononic devices. However, we have discovered that the edge states of acoustic topological insulators (ATIs) are not immune to all types of defects, even at subwavelength sizes. In contrast to the spin-mixing defects proposed in previous work [35], we have explored the effects of periodic defects that do not break the global $C_{6v}$ symmetry of the system on sound-wave transmission. We have discovered an anomalous phenomenon in which simply changing the angle of a single defect can significantly impact the transmission rate of sound waves. This phenomenon has rarely been investigated in previous works.

Furthermore, topological insulators have been increasingly utilized in the design of topological logical elements in photonic and phononic systems [36]. For example, two-dimensional photonic crystals have been used to construct topological all-optical logic gates [14] that exhibit strong topologically protected properties, even in the presence of significant disorders. By constructing topological and trivial photonic crystals, it is possible to realize pseudospin-preserving and -flipping edge states, leading to experimental observations of switched-ON and -OFF states [15]. In the acoustic domain, sound switches [29–31] are essential components of various logic gate designs, and recent research has focused on acoustic valley-Hall topological insulators for achieving XOR and OR logic functions [32,33]. However, previous works on topological sound switches (TSSs) have some limitations, such as only being applicable to a single frequency [31] or requiring rigorous conditions [29,30] like an appropriate temperature or pressure, which hinder their practical applications.

Here, we first investigate the effect of introducing periodic rhombus scatterer defects on the band structure of ATIs. Then, we replace one triangular scatterer of an ATI (the robust edge states of which were demonstrated previously [37]) with a rhombus rotator and find that the transmission of sound waves changes significantly with the rotation angle, even when there is only a single defect. This inspires us to consider the rotation angle of the defect as an alternative degree of freedom for easy control of acoustic wave transmission over a wide frequency range. Building on this concept, we develop a broadband TSS with a high transmission ratio before and after switching by simply rotating a single scatterer. Based on this TSS, we further experimentally design three topological acoustic

*Contact author: xyzou@nju.edu.cn

 

logic gates with high robustness to defects, which hold promise for applications in acoustic signal processing.

## II. TSS AND ITS TRANSMISSION-REGULATION EFFECT

As shown in Fig. 1(a), a pseudospin ATI, which consists of two types of honeycomb lattice array composed of triangular scatterers, is in the switched-OFF state. The unit cell of the ATI, as schematically shown in Fig. 1(b), has $C_6$ symmetry and the existence of the band gap is determined by the angles of the triangular scatterers. Previous work [37] has demonstrated that topologically protected edge states appear at the interface between these two types of honeycomb lattice presented in Fig. 1(a). However, when substituting one triangular scatterer located at the interface by a diamond-shaped one in the manner shown in Fig. 1(b), we observe a significant impact on the transmission of sound waves, depending on the rotation angles of this substitute. Specifically, as shown in Fig. 1(c), we use the horizontal rhombus (marked in gray) as the baseline of 0° rotation angle. Clockwise rotation gradually opens the switch until it reaches −60°, fully opening it (referred to as the "ON" state), resulting in high transmission of sound waves. Conversely, counterclockwise rotation to 60° fully closes the switch (referred to as the "OFF" state), leading to almost complete reflection of sound waves. Figure 1(c) presents a conceptual diagram of a physically realizable switch designed with the user-friendly feature of a TSS. The specific parameters are as follows: the lattice constant of each unit cell is $a = 60.0$ mm, the obtuse angle of the rhombus is $\alpha = 120°$, the side length of the triangular scatterer is $l = 14.9$ mm, and the side length of the rhombus scatterer is $b = 17.5$ mm.

To investigate the impact of the rotation angle of the rhombus defect on the transmission of pseudospin edge states, we utilize COMSOL Multiphysics to calculate the dispersion projection of supercells with five periods, as depicted in the left panel of Fig. 2. Subsequently, we examine the transmission of sound waves excited by a point source (frequency at the band gap) in a finite structure. Figures 2(a)–2(c) present the results without defects, with a TSS in the ON state, and with that in the OFF state, respectively. In the absence of any defects, five dispersion curves appear within the band gap due to the folding of the Brillouin zone. Adjacent dispersion curves degenerate at the high-symmetry point, and a tiny gap appears around 9.40 kHz, which is consistent with the projected dispersion curve of a supercell with only one period [37]. When a point source of 9.83 kHz is placed at the left entrance of the interface in the defect-free finite structure, the topologically protected edge states almost completely transmit through the structure, as shown in Fig. 2(a). Next, we replace one triangular scatterer at the interface with the rhombus one (the sound switch introduced earlier), and rotate it to the fully open position, i.e., the ON state. We repeat the previous process on the structure with the ON configuration and obtain the dispersion curve and transmission results. As shown in Fig. 2(b), the band structure of the ON configuration is almost the same as the one without defects, except for a slight opening at the degeneracy point. Therefore, it can be predicted that the transmission of this structure is very close to that without defects, as confirmed by the transmission graph, which indicates that the transmission of sound waves is hardly affected by the rhombus defect. In contrast, the dispersion curves of the OFF-configuration supercell, as shown in Fig. 2(c), appear to be very flat compared to when there are no defects, indicating group velocities close to zero, i.e., localized states. Correspondingly, the sound-pressure-level (SPL) field distribution shows that the sound-wave transmission is severely suppressed at this time. When the rotation

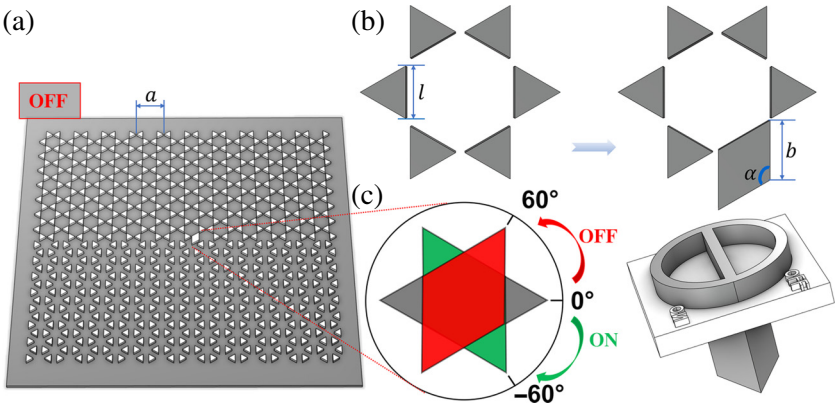


FIG. 1. (a) Schematic of the pseudospin ATI in which the rhombus TSS is in the OFF state. (b) Unit cell of the pseudospin ATI composed of six triangular scatterers. Proposed TSS is formed by replacing one of the triangular scatterers with a diamond-shaped one. (c) Enlarged view of the TSS and concept diagram of the actual switch design. With the gray rhombus as the reference for 0°, rotating clockwise 60° represents ON, and counterclockwise 60° represents OFF.

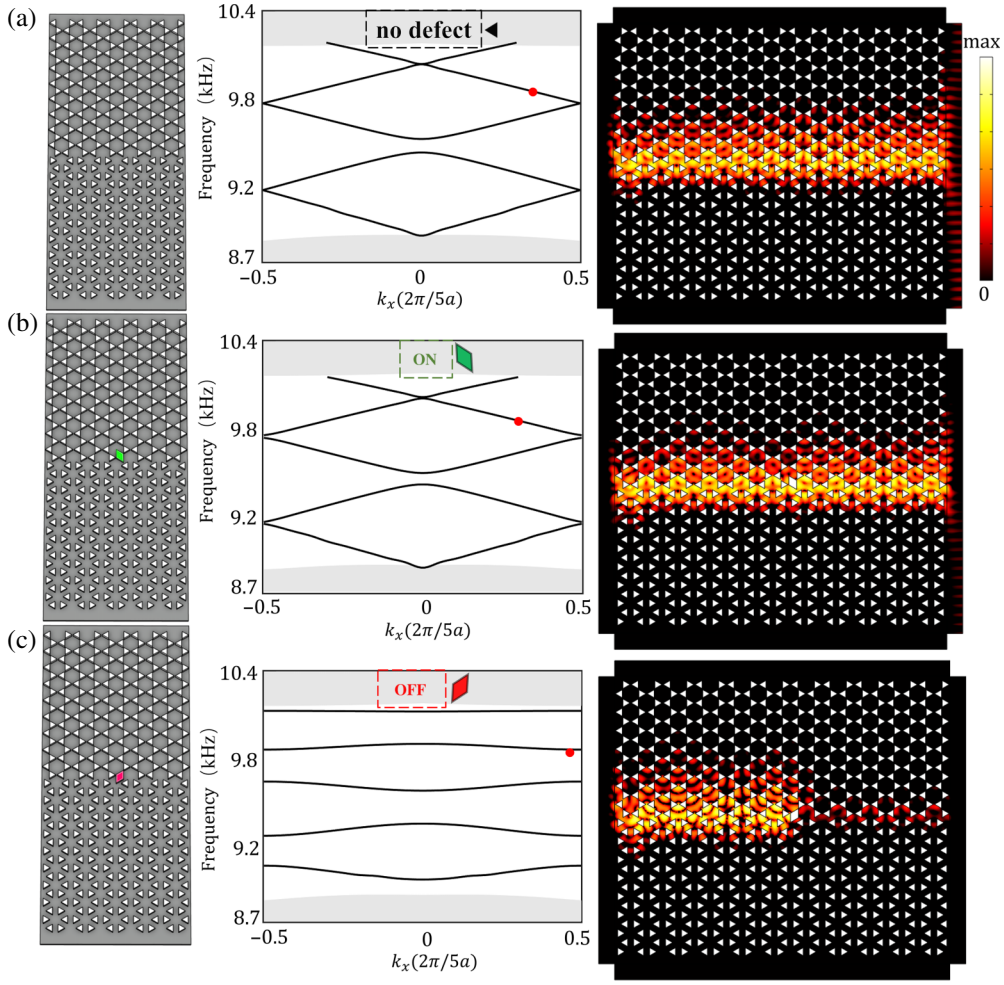


FIG. 2. Dispersion projection of the supercells with five periods and the simulated SPL field distributions in finite structures at 9.83 kHz. (a) Five-period supercell without TSS and its band structure. SPL field distribution shows that sound waves have high transmission rates in the finite structure without TSS due to topological protection. (b) Same as (a) but for the supercell with a TSS in the ON state. SPL field distribution shows that sound waves also have high transmission rates. (c) Same as (a) but for the supercell with a TSS in the OFF state. Distribution of the SPL field shows a significant suppression of sound-wave transmission due to TSS.

angle of the TSS deviates slightly from $-60°(60°)$, i.e., the ON (OFF) states, the sound-wave transmission SPL barely changes, indicating that the switching efficiency is robust to rotation-angle disorder. More detailed information can be found in Appendix D.

The pseudospin degeneracy in acoustic systems is not ensured by time-reversal symmetry, as phonons are bosons, but rather by crystal symmetry. This makes the acoustic pseudospin Hall insulator less robust compared to its electronic counterpart, which relies on global time-reversal symmetry to protect its band topology. Additionally, unlike electronic quantum spin Hall systems, acoustic pseudospin Hall systems exhibit a more fragile topology. Therefore, acoustic topological edge transports are not immune to all types of defects. For example, spin-mixing defects can induce backscattering [35,38]; this provides the possibility for the rhombus-defect-based TSS proposed here. From the perspective of crystal symmetry, which protects the edge states of fragile topological insulators [39], we could analyze how the TSS can significantly impact acoustic wave transmission and provide a straightforward explanation. Due to the zigzag shape of the boundary of the topological insulator, rather than a straight line, the TSS in the OFF state forms a rigid barrier at the boundary, while that in the ON state does not, although they can be transformed into each other by a simple rotation. When the switch is in the ON state, the lower part of the rhombus defect (located at the interface of two types of sonic crystals) is almost in the same position and size as the triangular scatterer without defects. So it hardly disrupts the crystal symmetry, resulting in a minimal influence on the coupling between unit cells. Conversely, when the switch is in the OFF state, the lower part of the rhombus is roughly mirror symmetric to the triangular scatterer,

which severely disrupts the local crystal symmetry and hinders the coupling between the two airborne atoms on each side, thereby forming an "electrical circuit break" (high impedance of inductance). The simulated vortical energy flux, i.e., acoustic pseudospin and the speed of sound flow both confirm the above analysis (see Appendix F for details). Inspired by previous work [22], we can use the simple one-dimensional periodic circuit model shown in Fig. 5 (see Appendix A) to abstractly simulate the switching effect of the TSS. Since there are acoustic vortices (so-called pseudospin) protected by crystal symmetry in each unit cell at the crystal interface [37], we can regard the airborne atoms in each unit cell as capacitors, $C$, and the coupling between them as inductance, $L$. Based on Kirchhoff's current law, when the switch is turned ON, the circuit equation can be expressed as

$$\begin{aligned}
\omega^2 U_1 &= -2(\mu+\mu)U_1 + \mu U_2 + \mu U_6 e^{i5\mathbf{k}a},\\
\omega^2 U_2 &= -2(\mu+\mu)U_2 + \mu U_1 + \mu U_3,\\
\omega^2 U_3 &= -2(\mu+\mu)U_3 + \mu U_2 + \mu U_4,\\
\omega^2 U_4 &= -2(\mu+\mu)U_4 + \mu U_3 + \mu U_5,\\
\omega^2 U_5 &= \mu U_6 e^{-i5\mathbf{k}a} - 2(\mu+\mu)U_5 + \mu U_6,
\end{aligned} \tag{1}$$

where $\mu = -(1/LC)$, and $\mathbf{k}, a, \omega$, and $U_i$ represent the Bloch wave vector, the aforementioned lattice constant, the angular frequency, and the electric pressure in the $i$th capacitor, respectively. Equation (1) can be rewritten as the vector form:

$$H_{\text{on}}\mathbf{U} = \omega^2\mathbf{U}, \tag{2}$$

where $\mathbf{U} = (U_1, U_2, U_3, U_4, U_5)$ and $H_{\text{on}}$ is the Hamiltonian of the ON system, which can be written as

$$H_{\text{on}} = \begin{bmatrix}
-2(\mu+\mu) & \mu & 0 & 0 & -\mu e^{i5\mathbf{k}a}\\
\mu & -2(\mu+\mu) & \mu & 0 & 0\\
0 & \mu & -2(\mu+\mu) & \mu & 0\\
0 & 0 & \mu & -2(\mu+\mu) & \mu\\
-\mu e^{-i5\mathbf{k}a} & 0 & 0 & \mu & -2(\mu+\mu)
\end{bmatrix}. \tag{3}$$

In contrast, with $\varepsilon$ representing a small quantity, the Hamiltonian of the OFF system,

$$H_{\text{off}} = \begin{bmatrix}
-2(\mu+\mu) & \mu & 0 & 0 & -\mu e^{i5\mathbf{k}a}\\
\mu & -2(\mu+\mu) & \mu & 0 & 0\\
0 & \mu & -2(\mu+\mu) & \varepsilon & 0\\
0 & 0 & \varepsilon & -2(\mu+\mu) & \mu\\
-\mu e^{-i5\mathbf{k}a} & 0 & 0 & \mu & -2(\mu+\mu)
\end{bmatrix}, \tag{4}$$

is different from $H_{\text{on}}$ due to the electrical circuit break between the third and fourth subunit cells. Diagonalization of these two Hamiltonians results in the corresponding dispersion curves shown in Figs. 5(b) and 5(c), which are very similar to those in Figs. 2(b) and 2(c). Therefore, we could regard the TSS in the OFF state as an acoustic rigid boundary for sound waves, and more details about the circuit model can be found in Appendix A.

## III. TOPOLOGICAL LOGIC GATES BASED ON TSSs

Based on this TSS, three types of topological logic gates are designed. As shown in Fig. 3, we define the states of two TSSs as $(S_1, S_2)$, where $S_i$ $(i = 1, 2)$ represents ON (encoded as 1) or OFF (encoded as 0). Figure 3(a) shows the AND gate containing two TSSs connected in series, with source $I$ placed at the left entrance of the interface, and the SPL detected at the right exit demonstrates the truth value of the output state. Through simulation calculations, we find that for the switch states $(0, 1)$ and $(1, 0)$, the sound energy at the exit is very weak, resulting in an output state of (0), i.e., false, as depicted in Fig. 3(b). However, for the state $(1, 1)$, the strong acoustic energy at the exit proves an output of (1), i.e., true, which demonstrates the effectiveness of this AND gate. Figure 3(c) shows the designed OR (XOR) gate consists of two parallel TSSs. According to the interference mechanism, when two input sources at $I_1$ and $I_2$ have the same amplitude and phase, the two sound waves interfere constructively, resulting in an OR gate. On the contrary, if there is a phase difference of $\pi$ between the sources, interference happens destructively, which makes

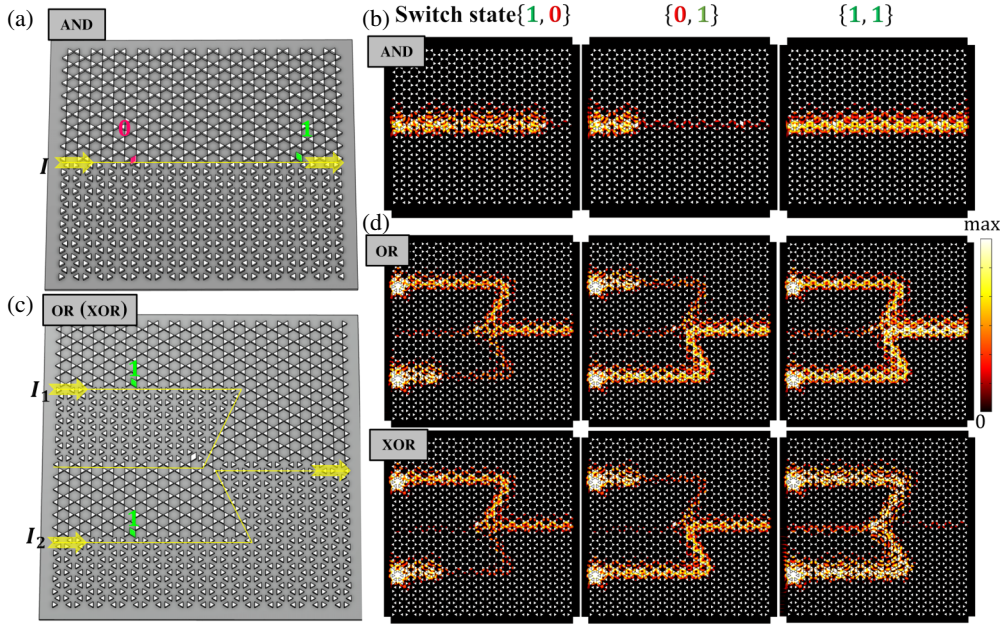


FIG. 3. Schematic diagram of topological acoustic logic gates and their simulated SPL field distributions in 9.83 kHz. Yellow lines represent the interfaces of two topologically distinct honeycomb arrays. (a) Schematic diagram of the AND gate. Sound waves are incident from entrance $I$, pass through two TSSs, and the intensity of the outgoing sound determines the truth value of the transmission signal. (b) Distribution of the SPL field shows that the output is true only when in the switch state is $(1, 1)$. (c) Schematic diagram of the OR (XOR) gate. Two sources are set at $I_1$ and $I_2$ with the same amplitude and a phase difference of $0(\pi)$, which corresponds to an OR (XOR) gate. (d) Distribution of the SPL field of OR and XOR gates.

it an XOR gate. The simulation results presented in Fig. 3(d) demonstrate excellent agreement with the predicted outcomes. We observe that for the OR gate, the sound energy that passes through the output port is evident for all three states, $(1, 0)$, $(0, 1)$, and $(1, 1)$, confirming that the outputs are true. In contrast, for the XOR gate, only the outputs for the states $(1, 0)$ and $(0, 1)$ are true, while the sound energy that passes through the output port for the state $(1, 1)$ is very weak, indicating a false output. In fact, a NOT gate can also be designed by utilizing interference mechanisms.

## IV. EXPERIMENTAL OBSERVATION OF THE EFFECT OF TSSs AND TOPOLOGICAL LOGICAL GATES

Next, we conduct experiments to verify the effectiveness of the proposed TSSs and the topological logic gates designed based on them. First, we experimentally measured the SPL of transmission on condition of different switch states within the frequency range from 9.0 to 11.1 kHz, as shown in Fig. 4(a). It can be observed that within a wide bandwidth of approximately 9.4–10.2 kHz, the difference in SPL measured at the exit between the ON and OFF states is over 12 dB, which demonstrates a relatively good performance for the TSS. Then, to experimentally demonstrate the logical functions of OR and XOR gates, we fabricated the experimental sample shown in Fig. 4(b). Two bits can be realized by the simple manipulation of rotating two TSSs in the sample, leading to four possible switch states of $(0, 1), (1, 0), (0, 0)$, and $(1, 1)$, which provide a flexible platform for logical computation. In the experiment, we uniformly set 85 dB as the threshold, meaning that the output state is (0) when the SPL probed at the exit is lower than this value, and (1) when higher. For the OR logic gate, we set two sound sources with the same initial phases and amplitudes at input ports $I_1$ and $I_2$. The output SPL at two frequencies, 9.74 and 10.1 kHz, are measured and the results are shown as the blue bars in Fig. 4(d). For comparison, for the XOR gate, we need to set two sound sources with the same amplitude but opposite initial phases at $I_1$ and $I_2$. It should be noted that during the experiment, different sound delays need to be set accordingly for different frequencies to maintain a phase difference of $\pi$. Also, we have measured the output SPLs at frequencies of 9.74 and 10.1 kHz, and the results are shown as the gray bars in Fig. 4(d). The bar charts show that for the OR gate, the only switch state that results in an output signal of (0) (i.e., lower than 85 dB) is $(0, 0)$ for both frequencies. Conversely, for the XOR gate, as long as the two switches are in the same state, either $(0, 0)$ or $(1, 1)$, the output state will be (0), which agrees well with the simulated result. This demonstrates that our proposed topological logic gates based on designed TSSs have good logic operation capabilities. To provide a clearer illustration of the logical functions of these topological

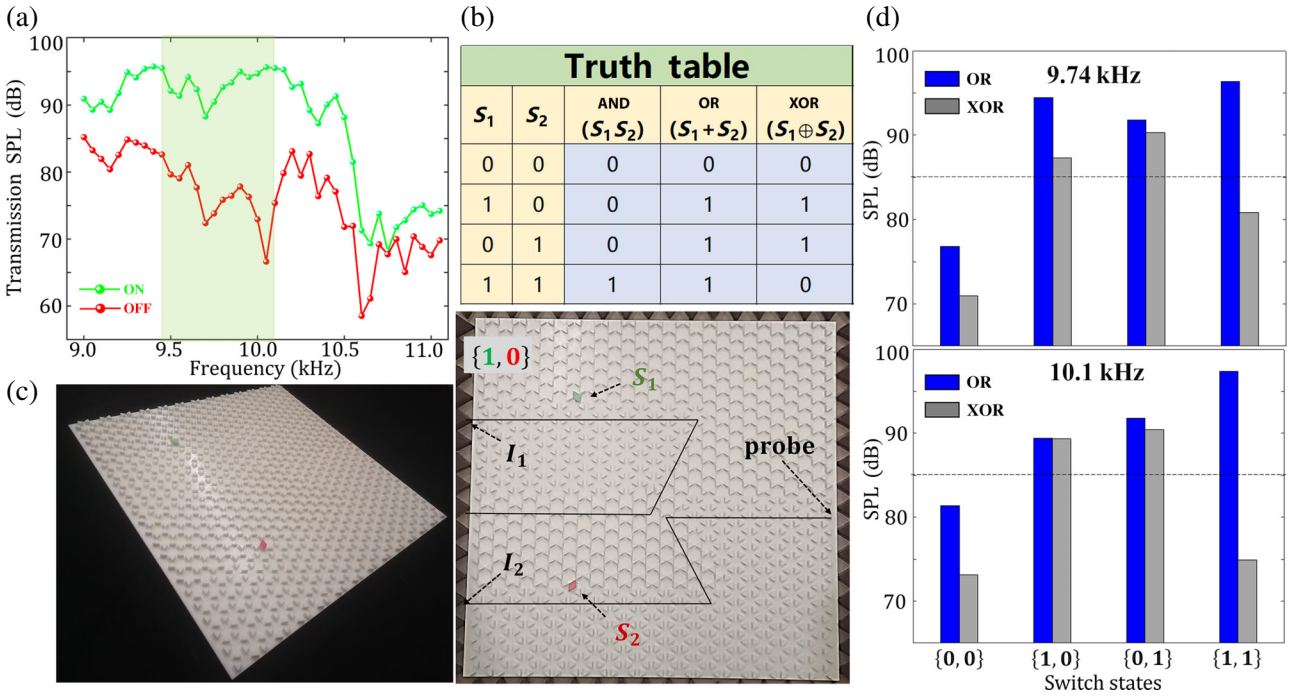


| $S_1$ | $S_2$ | AND $(S_1 S_2)$ | OR $(S_1+S_2)$ | XOR $(S_1 \oplus S_2)$ |
|---|---|---|---|---|
| 0 | 0 | 0 | 0 | 0 |
| 1 | 0 | 0 | 1 | 1 |
| 0 | 1 | 0 | 1 | 1 |
| 1 | 1 | 1 | 1 | 0 |

FIG. 4. (a) Experimentally measured SPL of transmitted sound waves in ON and OFF states of the TSS. Light green highlights the frequency band where the effect of TSS is significant. (b) Truth table for three topological logic gates. Left two columns represent the switch states ($S_1$, $S_2$), and right four columns represent the signal output states. (c) Schematic diagram of the experimental sample of the OR (XOR) gate in the $(1, 0)$ switch state. Two identical sound sources are placed at $I_1$ and $I_2$, and a probe is placed at the exit on the right side of the interface. (d) Output SPL measured at frequencies of 9.47 and 10.1 kHz. Blue and gray bars represent the measurement results of OR and XOR gates, respectively. Black dashed line is located at the threshold frequency of 85 dB.

logic gates, we have constructed a truth table based on our measurement results, as shown in Fig. 4(b). Notably, these gates are robust against certain disorders, thanks to the topologically protected edge state, and further details can be found in Appendix B.

## V. CONCLUSIONS

We replaced a triangular scatterer in a pseudospin ATI with a rhombus rotator and investigated the effect of the rotation angle on the transmission of edge states. Our results demonstrate that rotating the rhombus defect leads to a significant change in transmittance. Based on this, we developed a readily usable TSS with a SPL difference of more than 12 dB across a wide bandwidth. Notably, our TSS outperforms previous designs in terms of bandwidth, robustness, and simplicity. Furthermore, we encoded the ON and OFF states as binary digits 1 and 0, respectively, and designed three topological logic gates based on this encoding. The logical functionality of these gates was thoroughly validated through both simulations and experiments. These findings not only provide a practical platform for acoustic computing and signal processing but also hold potential for applications in photonic and phononic crystals by demonstrating the ability to control waves through a single defect.

Data that support the findings of this study are available from the corresponding author upon reasonable request.

## ACKNOWLEDGMENTS

This work was supported by the National Key Research and Development Program of China (Grant No. 2022YFB3204303), the National Natural Science Foundation of China (Grants No. 12074184, No. 12274219, and No. 11934009), and the Key Research and Development Project of Jiangsu Province (Grant No. BE2022814).

## APPENDIX A: ANALOGY TO CIRCUIT MODELS

We consider each airborne atom contained in the subunit cells of the five-period supercell as a Helmholtz resonator, and the air connecting the subunit cells as coupling tubes. Through this method, the scattering system in Fig. 5(a), i.e., the ATI with the TSS proposed in the manuscript, can be equivalently mapped to the resonant system in Fig. 5(b). By using classical electroacoustic analogy, the system in Fig. 5(b) can be analogized to the

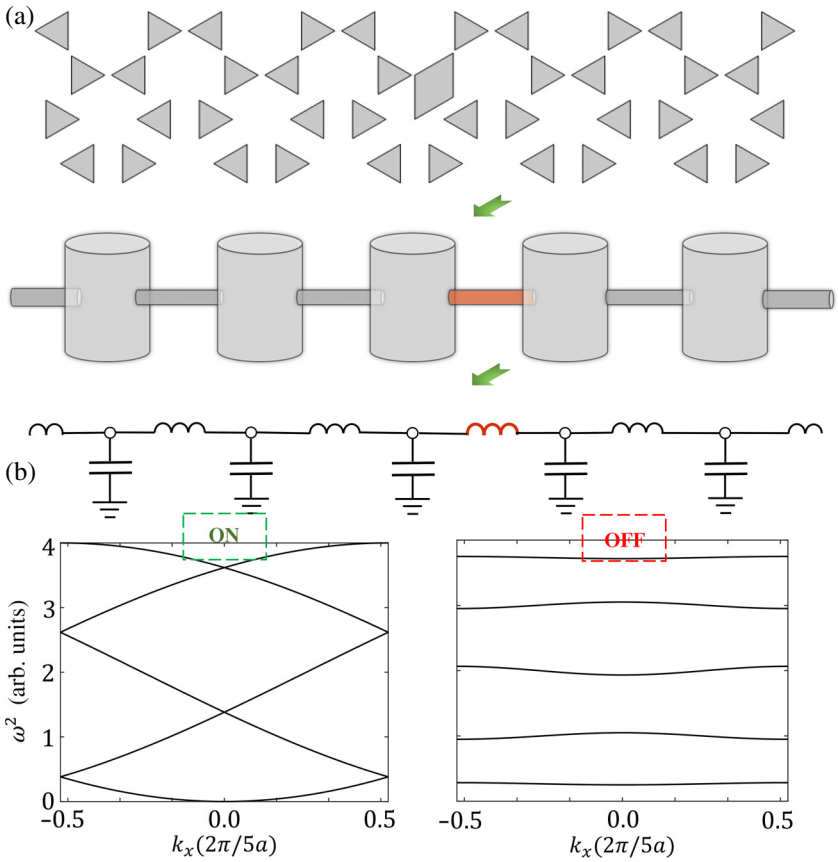


FIG. 5. (a) Schematic diagram of TSS proposed in the manuscript, which is the OFF state. (b) Schematic diagram of a cavity-resonance system equivalent to the five-period supercell. Inner part of the brown pipe is very slender, resulting in a very weak coupling between the third and fourth Helmholtz resonant cavities. (c) Equivalent circuit diagram, where the brown inductor has a strong inductance. (d) Band structures obtained by solving the Hamiltonian matrix of the circuit. Left and right figures correspond to the circuit in the "ON" state and in the proximity of the "OFF" state, respectively.

periodic circuit in Fig. 5(c), where the cavities are analogous to capacitors $C$ and the coupling tubes are analogous to inductances $l$. The TSS in the OFF state can block the coupling, which is equivalent to a very long and thin coupling tube, and this can be considered as a very large inductance (marked in brown) in the circuit [Fig. 5(b)]. We take the parameter values here as $C = -1, L = -1, \mu = -1/(LC) = -1$, and $\varepsilon = -0.1$ and obtain the circuit band structures corresponding to open and proximately closed circuits by diagonalizing the Hamiltonian matrices shown in Eqs. (3) and (4) of the main text, as shown in Fig. 5(d). Comparing them with Figs. 2(b) and 2(c) in the main text, we can see that the calculated and simulated band structures are very similar; this further demonstrates the effect of the TSS on sound waves.

It is worth noting that our analogy between the acoustic pseudospin Hall insulator and a circuit model differs from the classical electroacoustic analogy, as the scattering system here is not a lumped parameter system. However, since each unit cell has a robust acoustic vortex, we can treat it as a whole, equivalent to the capacitor mentioned earlier. Therefore, we did not determine the capacitance and inductance values based on structural parameters, but rather used a numerical value of $-1$ as a parameter in the Hamiltonian matrix. This abstract analogy helps us understand that the functionality of the TSS arises from its blocking of the coupling between acoustic cavities.

## APPENDIX B: THE ROBUSTNESS OF THE TOPOLOGICAL GATES AGAINST DISORDER

To investigate the robustness of the proposed topological logic gates against defects, we introduced "inverted-V" defects to three types of logic gates and observed their output truth values. We introduced defects into both the $(0, 1)$ and $(1, 1)$ switch states and compared them with defect-free cases, as shown in Fig. 6. It can be seen clearly that for each logic gate, the introduced defects have no effect on the result, regardless of whether the output is in the state of 0 or 1, i.e., the output SPL remains almost unchanged. In other words, the logical functions of the three types of logic gates designed here are immune to defects of appropriate strength, and this broadens the design horizon for more complex topological logic gates.

## APPENDIX C: THE BROADBAND CHARACTERISTIC OF THE TOPOLOGICAL SOUND SWITCH

To demonstrate the broadband characteristics of the TSS, we simulate the SPL distributions under different frequencies when the TSS is in the ON and OFF states. In addition to the 9.83-kHz result shown in Fig. 2 of the main text, Fig. 7 also shows that the TSS has good tunable control over sound-wave transmission rates at multiple frequencies, including 9.4, 9.7, and 10.0 kHz.

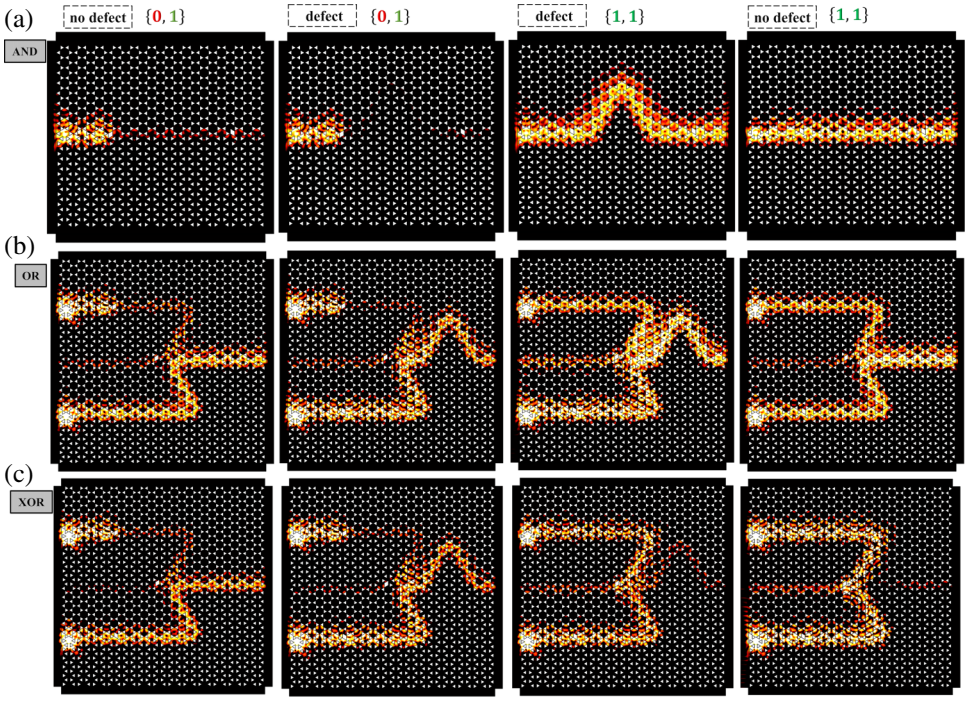


FIG. 6. (a) Distribution of the SPL field for the AND gate with and without an inverted V-shaped defect at $(0, 1)$ and $(1, 1)$ states, respectively. (b) Same as (a) but for the OR gate. (c) Same as (a) but for the XOR gate. Results show that the introduction of defects does not affect the truth value of the output signal for both the $(0, 1)$ and $(1, 1)$ switch states.

Furthermore, we simulate the sound transmission rates from 9.0 to 11.0 kHz, and the results are shown in Fig. 8, indicating that the TSS has good tunable control over sound-wave transmission within the broad frequency range of 9.4 to 10.2 kHz (shaded in light green). This is in good agreement with the experimentally measured transmission rates shown in Fig. 4(a) of the main text. Both the simulation and experimental results demonstrate the broadband characteristics of the TSS proposed here.

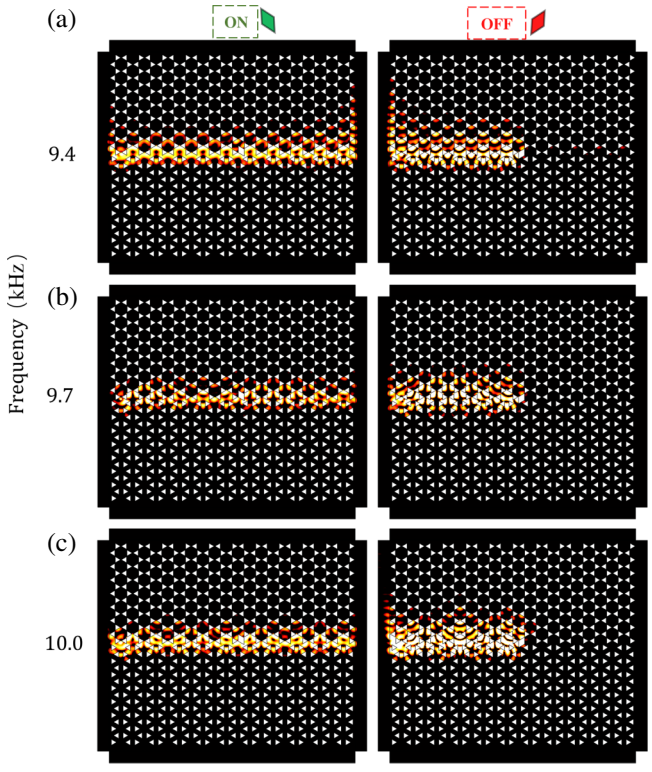


FIG. 7. SPL field distributions when TSS is in the ON and OFF states, with the sound-source frequency at (a) 9.4, (b) 9.7, and (c) 10.0 kHz.

## APPENDIX D: THE VARIATION OF TRANSMISSION RATE WITH ROTATION ANGLE

To further validate the robustness of the switching effect of TSSs to the rotation angle in the ON and OFF states, we

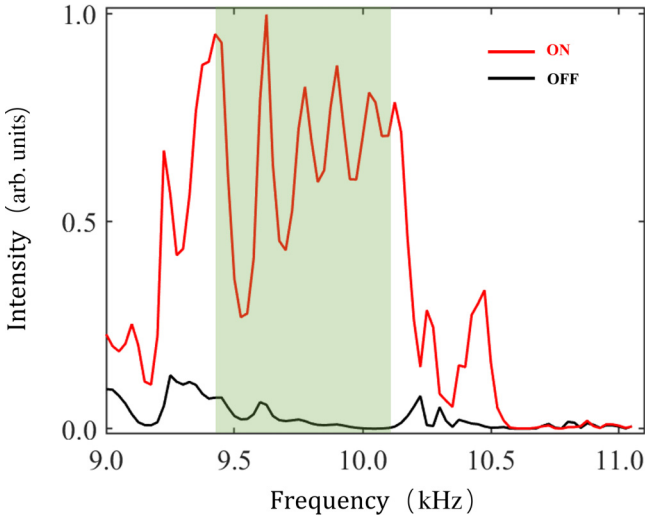


FIG. 8. Normalized sound-transmission spectrum from 9.0 to 11.0 kHz, with the red line and black line, respectively, marking the results of TSS in the ON and OFF states.

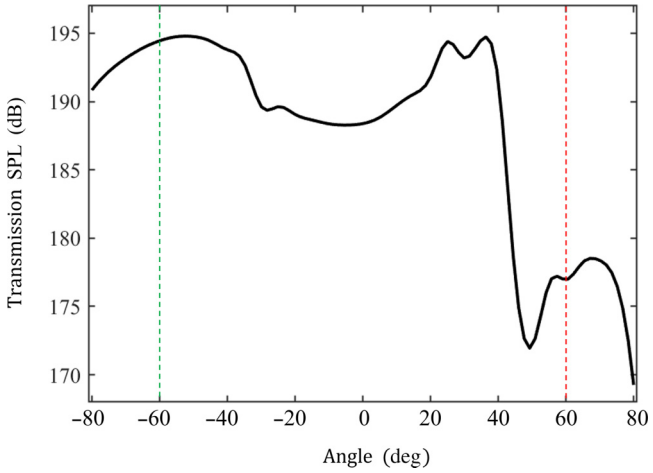


FIG. 9. Variation of the system's transmission with rotation angle (with the frequency fixed at 9.83 kHz). When the rotation angle does not significantly deviate from $-60°(60°)$, sound-pressure-level transmission rate remains stable at a relatively high (low) level.

simulated the transmission rate of the 9.83 - kHz sound signal. The result is shown in Fig. 9, where the transmission SPL undergoes a sharp decline when the rotation angle of the TSS changes from 38° to 50°. For angles other than this, the transmission changes very smoothly, especially around $-60°$ and $60°$, where the transmission SPL is quite insensitive to changes of the rotation angle, indicating that the sound-wave-control effect is robust to rotation-angle disorder when the TSS is in the ON $(-60°)$ or OFF $(60°)$ state.

It is worth noting that the sharp valley here (between 38° and 50°) is caused by the coupling between topological edge state and the acoustic cavity. In the model proposed here, the defect unit cell can be regarded as an acoustic cavity, the coupling of which with the incident sound wave is of the $\delta$ type (relevant theory can be found in Ref. [39]). When the frequency of the topological edge state matches the eigenfrequency of the acoustic cavity, the resonance will confine the sound energy within the cavity, leading to a sharp decrease in transmittance, as shown in Fig. 9. Although this mechanism differs from that of the TSS, it will not affect its application effect.

## APPENDIX E: TOPOLOGICAL SOUND SWITCHES WITH DIFFERENT GEOMETRIES

To further demonstrate the shape independence of the TSS's acoustic-wave-control effect proposed here, we

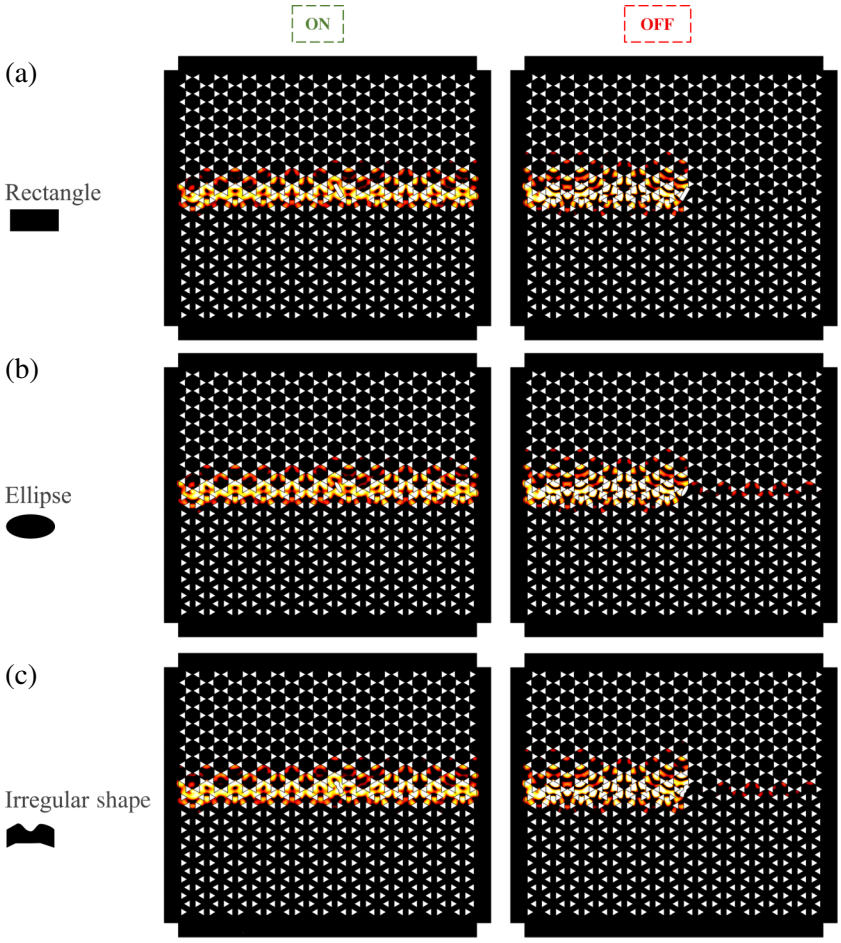


FIG. 10. SPL field distributions when TSS is in the ON and OFF states, if we replace the rhombus defect with similar-sized (a) rectangles, (b) ellipses, and (c) irregular shapes.

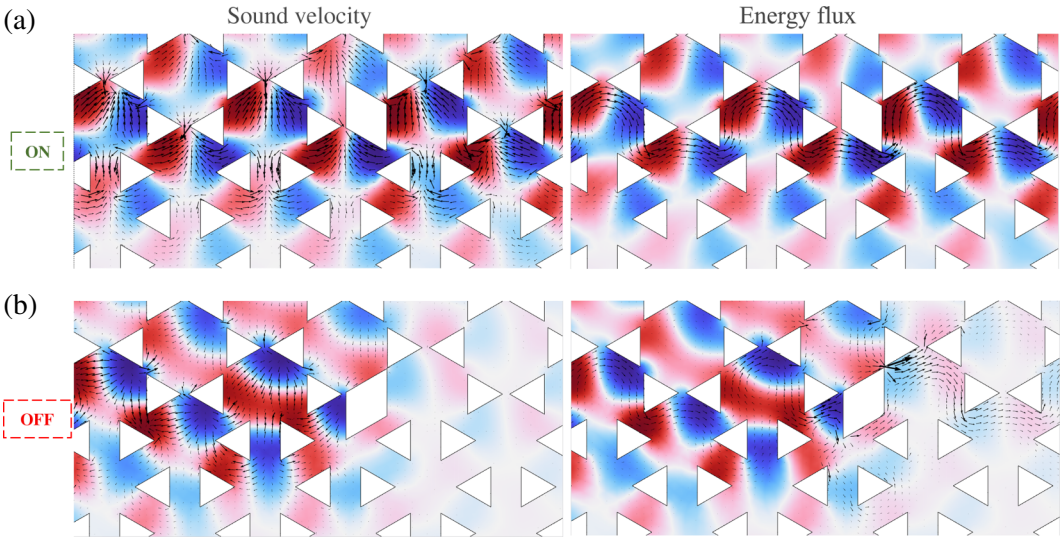


FIG. 11. Total sound-velocity and energy-flux distribution around TSS when it is in the (a) ON and (b) OFF states.

replaced the rhombus-shaped scatterer with similarly sized rectangular, elliptical, and irregularly shaped scatterers and simulated the transmission SPL distribution of a 9.83 - kHz sound signal. As shown in Fig. 10, for these three differently shaped TSSs, similar to the rhombus-shaped TSS proposed in the main text, when they are in the ON state, the sound-wave transmission is almost unaffected, whereas when they are in the OFF state, the sound-wave transmission is severely suppressed. The simulation results demonstrate that, as long as the TSS proposed here maintains a roughly oblong shape, it can exhibit sound-wave-control effects very close to those of the rhombus shape, indicating that the switching ability of the TSS is robust against shape variations.

## APPENDIX F: SOUND VELOCITY AND ENERGY FLUX

To visually explain why the rhombus defect proposed in the main text can significantly affect the transmission of sound waves, we simulated the energy flux and speed of sound when the TSS was in the ON and OFF states, as shown in Fig. 11. The simulation results show that when the TSS is in the ON state, the energy flux and speed of sound of the topological boundary state are hardly affected by the defect, because the crystal symmetry is not broken. On the contrary, when the TSS is in the OFF state, the lower part of the defect forms a mirror symmetry along the vertical direction with the triangular scatterer on the path of the edge state, thus severely breaking the local crystal symmetry. As a result, the edge state loses the protection of crystal symmetry, and the rhombus scatterer defects act like a hard barrier, reflecting the majority of sound energy back.

This phenomenon demonstrates that the acoustic pseudospin Hall insulator is a fragile topological insulator protected by crystal symmetry, with less robustness compared to its electronic counterpart protected by time-reversal symmetry.

[1] M. Z. Hasan and C. L. Kane, *Colloquium*: Topological insulators, Rev. Mod. Phys. **82**, 3045 (2010).
[2] R. Yu, W. Zhang, H.-J. Zhang, S.-C. Zhang, X. Dai, and Z. Fang, Quantized anomalous Hall effect in magnetic topological insulators, Science **329**, 61 (2010).
[3] X.-L. Qi and S.-C. Zhang, Topological insulators and superconductors, Rev. Mod. Phys. **83**, 1057 (2011).
[4] W. A. Benalcazar, B. A. Bernevig, and T. L. Hughes, Electric multipole moments, topological multipole moment pumping, and chiral hinge states in crystalline insulators, Phys. Rev. B **96**, 245115 (2017).
[5] W. A. Benalcazar, B. A. Bernevig, and T. L. Hughes, Quantized electric multipole insulators, Science **357**, 61 (2017).
[6] J. Langbehn, Y. Peng, L. Trifunovic, F. von Oppen, and P. W. Brouwer, Reflection-symmetric second-order topological insulators and superconductors, Phys. Rev. Lett. **119**, 246401 (2017).
[7] F. Liu and K. Wakabayashi, Novel topological phase with a zero Berry curvature, Phys. Rev. Lett. **118**, 076803 (2017).
[8] Z. Song, Z. Fang, and C. Fang, $(d-2)$-Dimensional edge states of rotation symmetry protected topological states, Phys. Rev. Lett. **119**, 246402 (2017).
[9] M. Ezawa, Higher-order topological insulators and semimetals on the breathing kagome and pyrochlore lattices, Phys. Rev. Lett. **120**, 026801 (2018).
[10] F. Schindler, A. M. Cook, M. G. Vergniory, Z. Wang, S. S. P. Parkin, B. A. Bernevig, and T. Neupert, Higher-order topological insulators, Sci. Adv. **4**, eaat0346 (2018).

[11] J. Noh, W. A. Benalcazar, S. Huang, M. J. Collins, K. P. Chen, T. L. Hughes, and M. C. Rechtsman, Topological protection of photonic mid-gap defect modes, Nat. Photonics **12**, 408 (2018).

[12] C. W. Peterson, W. A. Benalcazar, T. L. Hughes, and G. Bahl, A quantized microwave quadrupole insulator with topologically protected corner states, Nature **555**, 346 (2018).

[13] B.-Y. Xie, H.-F. Wang, H.-X. Wang, X.-Y. Zhu, J.-H. Jiang, M.-H. Lu, and Y.-F. Chen, Second-order photonic topological insulator with corner states, Phys. Rev. B **98**, 205147 (2018).

[14] L. He, W. Zhang, and X. Zhang, Topological all-optical logic gates based on two-dimensional photonic crystals, Opt. Express **27**, 25841 (2019).

[15] Y. Yang, X. Qian, L. Shi, X. Shen, Y. Wang, and Z. H. Hang, Observation and control of pseudospin switching in a finite-width topological photonic crystal, Opt. Express **30**, 5731 (2022).

[16] M. Serra-Garcia, V. Peri, R. Süsstrunk, O. R. Bilal, T. Larsen, L. G. Villanueva, and S. D. Huber, Observation of a phononic quadrupole topological insulator, Nature **555**, 342 (2018).

[17] H. Fan, B. Xia, L. Tong, S. Zheng, and D. Yu, Elastic higher-order topological insulator with topologically protected corner states, Phys. Rev. Lett. **122**, 204301 (2019).

[18] Z. Wang, Q. Wei, H.-Y. Xu, and D.-J. Wu, A higher-order topological insulator with wide bandgaps in Lamb-wave systems, J. Appl. Phys. **127**, 075105 (2020).

[19] Z.-G. Chen, C. Xu, R. Al Jahdali, J. Mei, and Y. Wu, Corner states in a second-order acoustic topological insulator as bound states in the continuum, Phys. Rev. B **100**, 075120 (2019).

[20] X. Ni, M. Weiner, A. Alù, and A. B. Khanikae, Observation of higher-order topological acoustic states protected by generalized chiral symmetry, Nat. Mater. **18**, 113 (2019).

[21] H. Xue, Y. Yang, F. Gao, Y. Chong, and B. Zhang, Realization of an acoustic third-order topological insulator, Nat. Mater. **18**, 108 (2019).

[22] C. Chen, T.-N. Chen, W. Ding, F.-Y. Yang, J. Zhu, and J. Yao, Impurity-induced multi-bit acoustic topological system, Int. J. Mech. Sci. **247**, 108183 (2023).

[23] Junxiang Fan, Bo Song, Lei Zhang, Xiaobo Wang, Zhi Zhang, Shuaishuai Wei, Xiao Xiang, Xuefeng Zhu, and Yusheng Shi, Structural design and additive manufacturing of multifunctional metamaterials with low-frequency sound absorption and load-bearing performances, Int. J. Mech. Sci. **238**, 107848 (2023).

[24] Y. Qi, C. Qiu, M. Xiao, H. He, M. Ke, and Z. Liu, Acoustic realization of quadrupole topological insulators, Phys. Rev. Lett. **124**, 206601 (2020).

[25] Z. Zhang, H. Long, C. Liu, C. Shao, Y. Cheng, X. Liu, and J. Christensen, Deep-subwavelength holey acoustic second-order topological insulators, Adv. Mater. **31**, 1904682 (2019).

[26] H. Li, Z. Wang, Z. Wang, C. Deng, J., Luo, J., Huang, X. Wang, and H. Yang, Acoustic multichannel transports of valley edge states in bilayer sonic crystals, Appl. Phys. Lett. **121**, 243101 (2022).

[27] D. Jia, H.-X. Sun, J.-P. Xia, S.-Q. Yuan, X.-J. Liu, and C. Zhang, Temperature-controlled tunable underwater acoustic topological insulators, New J. Phys. **20**, 093027 (2018).

[28] M. Wang, W. Zhou, L. Bi, C. Qiu, M. Ke, and Z. Liu, Valley-locked waveguide transport in acoustic heterostructures, Nat. Commun. **11**, 3000 (2020).

[29] H. Pirie, S. Sadhuka, J. Wang, R. Andrei, and J. E. Hoffman, Topological phononic logic, Phys. Rev. Lett. **128**, 015501 (2022).

[30] H.-Q. Dai, P. Xue, E.-H. Lu, L. Wang, and L.-Sh. Zhou, Experimental realization of a soft topological acoustic switch, Phys. Rev. B **107**, 144105 (2023).

[31] Q. Li, X. Xiang, L. Ye, W. Li, Y. Huang, and X. Wang, Topological ventilated sound switch from acoustic Su-Schrieffer–Heeger model, Appl. Phys. Lett. **122**, 191704 (2023).

[32] Z. Wang, Y. Yang, H. Li, J. Luo, J. Huang, Zh. Wang, B. Jiang, N. Yang, G. Jin, and H. Yang, Multichannel topological transport in an acoustic valley Hall insulator, Phys. Rev. Appl. **15**, 024019 (2021).

[33] Y.-J. Lu, Y. Wang, Y. Ge, S.-Q. Yuan, D. Jia, H.-X. Sun, and X.-J. Liu, Multifunctional acoustic logic gates by valley sonic crystals, Appl. Phys. Lett. **121**, 123506 (2022).

[34] A.-Y. Guan, Z.-Z. Yang, X. Zou, and J. Cheng, Controlling sound wave propagation in topological crystalline insulators and rainbow-trapping, Phys. Rev. Appl. **15**, 064056 (2021).

[35] Y.-C. Deng, H. Ge, Y. Tian, M.-H. Lu, and Y. Jing, Observation of zone folding induced acoustic topological insulators and the role of spin-mixing defects, Phys. Rev. B **96**, 184305 (2017).

[36] T. Mei, Z.-Q. Meng, K.-J. Zhao, and C.-Q. Chen, A mechanical metamaterial with reprogrammable logical functions, Nat. Commun. **12**, 7234 (2021).

[37] J. Ding, H.-X. Sun, J.-P. Xia, S.-Q. Yuan, X.-J. Liu, and C. Zhang, Acoustic topological insulator by honeycomb sonic crystals with direct and indirect band gaps, New J. Phys. **20**, 093027 (2018).

[38] C. Ji, Y. Zhang, Y. Liao, X. Zhou, J. Jiang, B. Zou, and Y. Yao, Fragile topologically protected perfect reflection for acoustic waves, Phys. Rev. Res. **2**, 01313 (2020).

[39] H.-X. Wang, G.-Y. Guo, and J.-H. Jiang, Band topology in classical waves: Wilson-loop approach to topological numbers and fragile topology, New J. Phys. **21**, 093029 (2019).